Electronic Supplementary Material (ESI) for ChemComm.

Supporting Information for: Design and photoisomerization dynamics of a new family of synthetic 2-stroke light driven molecular rotary motors

Michael Filatov,[*,†] Marco Paolino,[‡] Seung Kyu Min,[¶] and Cheol Ho Choi[†]

†*Department of Chemistry, Kyungpook National University, Daegu 702-701, South Korea*

‡*Dipartimento di Biotecnologie, Chimica e Farmacia (Dipartimento di Eccellenza 2018-2022), Università di Siena, Via A. Moro 2, 53100 Siena, Italy*

¶*Department of Chemistry, School of Natural Sciences, Ulsan National Institute of Science and Technology, Ulsan 44919, South Korea*

E-mail: mike.filatov@gmail.com

Contents

1 Proposed synthetic strategy

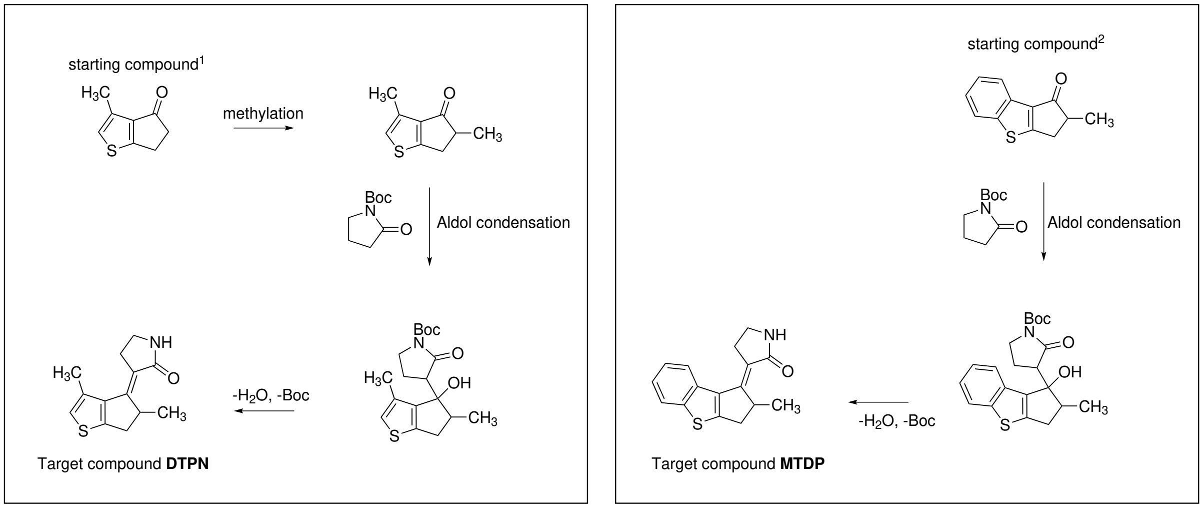

Scheme SI-1: Proposed strategy for the synthesis of the DTPN target compound (left panel) and its analogous compound MTDP (right panel).

In this section, we propose a strategy for the synthesis of the target compound (DTPN: 3-(3,5-dimethyl-5,6-dihydro-4H-cyclopenta[b]thiophen-4-ylidene)pyrrolidin-2-one) studied in the main text as well as its analogous compound (MTDP: 3-(4-Methyl-7-thiatricyclo [6.4.0.02,6]dodeca-1(8),2(6),9,11-tetraen-3-ylidene)pyrrolidin-2-one). Modifying the strategy previously used to synthesize the bio-mimetic photo-switch[1] **1** (see the main text) and combining it with the literature data, synthetic route to DTPN is derived and presented in Scheme SI-1. In particular, monomethylation in the α-position of the carbonyl group of the starting material 5,6-dihydro-4H-cyclopenta[b]thiophen-4-one (previously reported by Pinna et al. in Ref. 2) should easily provide the chiral compound 3,5-dimethyl-5,6-dihydro-4H-cyclopenta[b]thiophen-4-one (precursor of the stator blade) as a racemic mixture. The latter compound was also reported in a 2003 patent by Ewen et al.;[3] thus confirming its feasibility.

The monomethylated synthetic intermediate can be conjugated to the commercially available N-Boc pyrrolidinone by aldol condensation to obtain a mixture of diastereomers which, after treatment with an organic acid (e.g. TFA) can easily provide the DTPN target compound due to the simultaneous dehydration and elimination of the Boc protecting group. Then, the racemic mixture of E-DTPN or Z-DTPN should be separated by HPLC equipped with the chiral column.

Using a similar synthetic strategy, a series of related compounds can be prepared as well; *e.g.*, the MTDP compound shown in the background (gray color) of Scheme SI-1. This compound, deriving from the starting material 2-methyl-2,3-dihydro-1H-benzo[b] cyclopenta[d]thiophen-1-one previously reported by Landaluce et al.,[4] could be an interesting derivative of the DTPN motor in which the methyl group in position 3 of the stator is replaced by a condensed benzene ring. As deemed needed for practical applications, substitutions at various positions of the stator and/or the rotor blade of the DTPN and MTDP motors can be performed; thus paving a way to synthesizing a whole new family of molecular motors.

2 Computational methods

2.1 SSR method

The SSR method[5–10] employed in this work to obtain the ground and excited electronic states energies, forces on the nuclei (the analytic gradient), and the non-adiabatic coupling (NAC) vector employs ground state eDFT[11–16] to describe the non-dynamic electron correlation occurring due to multireference character of the ground state and eDFT for ensembles of ground and excited states[17–20] to obtain excitation energies from a variational time-independent formalism. The ensemble representation of the density and energy of a strongly correlated electronic state results in occurrence of the fractional occupation numbers (FONs) of several frontier KS orbitals. Here, the SSR(2,2) method is used, where two fractionally occupied orbitals accommodate two electrons in total. The energies of the ground S_0 and excited S_1 states are obtained in SSR(2,2) from variational optimization of an ensemble of a perfectly spin-paired singlet (PPS) electronic configuration and an open-shell singlet (OSS) configuration with respect to the KS orbitals and their FONs (the SA-REKS(2,2)[7] orbital optimization), which is followed by solving a 2×2 secular problem

$$\begin{pmatrix} E_0^{PPS} & \Delta_{01}^{SA} \\ \Delta_{01}^{SA} & E_1^{OSS} \end{pmatrix} \begin{pmatrix} a_{00} & a_{01} \\ a_{10} & a_{11} \end{pmatrix} = \begin{pmatrix} E_{S_0} & 0 \\ 0 & E_{S_1} \end{pmatrix} \begin{pmatrix} a_{00} & a_{01} \\ a_{10} & a_{11} \end{pmatrix} \tag{SI-1}$$

for the actual S_0 and S_1 states.[8–10] The interstate coupling parameter Δ_{01}^{SA} is calculated simultaneously with the E_0^{PPS} and E_1^{OSS} energies when optimizing the KS orbitals (and their FONs) in the SA-REKS(2,2) calculation.[8–10]

The analytic gradients of the S_0 and S_1 energies are calculated using the formalism of Ref. 21. The gradients of the S_0 and S_1 states are related to the gradients of the PPS and OSS states and the coupling element Δ_{01}^{SA} as

$$\boldsymbol{\nabla} E_{S_k} = a_{kk}^2 \boldsymbol{\nabla} E_0^{PPS} + a_{lk}^2 \boldsymbol{\nabla} E_1^{OSS} + 2\, a_{kk}\, a_{lk}\, \boldsymbol{\nabla} \Delta_{01}^{SA}\,; \quad l \neq k\,; \quad l,k = 0,1 \tag{SI-2}$$

From the gradients ∇E_{S_k} and $\nabla \Delta_{01}^{SA}$, the NAC vector $\mathbf{H}_{01}$ between S_0 and S_1 is calculated as

$$\mathbf{H}_{01} = \frac{1}{E_{S_1} - E_{S_0}} \left(\frac{2\, a_{00}\, a_{01}\, \mathbf{G}_{01} + \mathbf{h}_{01}}{a_{00}\, a_{11} + a_{01}\, a_{10}} \right), \tag{SI-3}$$

where

$$\mathbf{G}_{01} = \frac{1}{2}(\nabla E_{S_0} - \nabla E_{S_1}) \tag{SI-4}$$

$$\mathbf{h}_{01} = \nabla \Delta_{01}^{SA} \tag{SI-5}$$

$$\mathbf{g}_{01} = \frac{1}{2}(\nabla E_0^{PPS} - \nabla E_1^{OSS})\,. \tag{SI-6}$$

2.2 DISH-XF method

A detailed description of the DISH-XF method[22] can be found in the original article and the references cited therein. Here, a brief account of its basic features is given. The DISH-XF method combines the electronic equations derived from the exact factorization of the electronic-nuclear wavefunction[23–27] with the conventional TSH formalism.[28] The exact factorization enables one to seamlessly incorporate the effect of nuclear quantum momentum, which depends on the shape of nuclear distribution, into the classical equations of motion for the nuclei.

DISH-XF is a mixed quantum-classical method where the electronic degrees of freedom are treated quantum mechanically and the classical description in terms of trajectories is used for the nuclear degrees of freedom. For a given nuclear trajectory $\mathbf{R}^{(I)}$, the time-dependent electronic wavefunction $\Phi_{\mathbf{R^{(I)}}}(\mathbf{r}, t)$ is expanded in terms of the wavefunctions of the Born-Oppenheimer (BO) states as $\Phi_{\mathbf{R^{(I)}}}(\mathbf{r}, t) = \sum_l C_l^{(I)}(t)\phi_l(\mathbf{r}; \mathbf{R}^{(I)}(t))$ and the time evolution of an element $\rho_{lk}^{(I)}(t) = C_l^{(I)*}(t)C_k^{(I)}(t)$ of the reduced density matrix $\rho^{(I)}(t)$ is described by

$$\begin{aligned}\frac{d}{dt}\rho_{lk}^{(I)}(t) =& \frac{i}{\hbar}\left\{E_l^{(I)}(t) - E_k^{(I)}(t)\right\}\rho_{lk}^{(I)}(t) - \sum_j \left\{\sigma_{lj}^{(I)}(t)\rho_{jk}^{(I)}(t) - \rho_{lj}^{(I)}(t)\sigma_{jk}^{(I)}(t)\right\} \\ &+ \sum_j \left\{Q_{jl}^{(I)}(t) + Q_{jk}^{(I)}(t)\right\}\rho_{lj}^{(I)}(t)\rho_{jk}^{(I)}(t)\end{aligned} \tag{SI-7}$$

where $E_l^{(I)}$ and $\phi_l(\mathbf{r}; \mathbf{R}^{(I)}(t))$ are the energy and the wavefunction of the l-th BO state, $\sigma_{jk}^{(I)}$ is a non-adiabatic coupling matrix element between the jth and kth BO electronic states, and $Q_{jk}^{(I)}$ is a term that gives quantum correction to the nuclear motion arising from electronic-nuclear correlations;[25–27] the latter term is derived from the exact factorization of the electronic-nuclear wavefunction.[22] In Eq. (SI-7),the superscript (I) indicates a quantity obtained at the nuclear configuration $\mathbf{R}^{(I)}$.

In Eq. (SI-7), the $Q_{jk}^{(I)}$ term yields coupling between the nuclear quantum momenta $i\hbar\nabla_\nu|\chi|/|\chi|$ and the electronic phases $\mathbf{f}_{\nu,j}^{(I)}$ and $\mathbf{f}_{\nu,k}^{(I)}$

$$Q_{jk}^{(I)} = \sum_\nu \frac{i\hbar}{M_\nu} \frac{\nabla_\nu|\chi|}{|\chi|}\bigg|_{\mathbf{R}^{(I)}(t)} \cdot \left(\mathbf{f}_{\nu,j}^{(I)} - \mathbf{f}_{\nu,k}^{(I)}\right) \tag{SI-8}$$

where M_ν is a mass of the νth nucleus. The nuclear quantum momenta are obtained from a number of auxiliary nuclear trajectories generated for electronic states other than the running state l. Although the concept of auxiliary trajectories for decoherence-induced surface hopping dynamics is not new,[29] the correction used here is derived from the exact quantum equations and no further renormalization of the electronic density matrix is needed.

An auxiliary trajectory $\mathbf{R}^{(I)}(t')$ is generated when a nonzero $\rho_{kk}(t')$ is encountered at a time t' and is evolved classically with a uniform velocity obtained from the energy conservation law. The electronic phase term $\mathbf{f}_{\nu,k}^{(I)} = -\int^t \nabla_\nu E_k^{(I)}(t')dt'$ is evaluated by time integration of the momentum changes at the kth BO state. To calculate the quantum momentum, a fictitious Gaussian nuclear density $|\chi_k|^2$ with a uniform variance σ is associated with the auxiliary trajectory at each BO state. Then, the nuclear quantum momentum is $\nabla_\nu|\chi|/|\chi|(\mathbf{R^{(I)}(t)}) = -\frac{1}{2\sigma^2}(R_\nu^{(I)}(t) - \langle R_\nu^{(I)}(t)\rangle)$, where $\langle R_\nu^{(I)}(t)\rangle = \sum_k \rho_{kk}^{(I)} R_{k\nu}^{(I)}(t)$. The uniform variance σ can be either obtained from the initial distribution of nuclear trajectories or set as a parameter. Here, a uniform value $\sigma = 0.1$ a.u. is used.

Nuclear trajectories follow the Newtonian equations of motion on the PES of the running state l, *i.e.*, the force on the νth nucleus is $\mathbf{F}_\nu^{(I)} = -\nabla_\nu E_l^{(I)}$. When the surface hop probability becomes greater than a random number, a surface hop is initiated. The surface hop probability from the running state l to another state $k(\neq l)$ at a time interval $[t, t+\Delta t]$ is calculated as

$$P_{l\to k} = \frac{2\Re\left[\rho_{lk}^{(I)}(t)\sigma_{lk}^{(I)}(t)\right]}{\rho_{ll}^{(I)}(t)}\Delta t\,, \tag{SI-9}$$

where the same constraints as in the Tully's fewest switches algorithm[28,30] are imposed on the hopping transition; *i.e.*, when $E_k^{(I)}$ is greater than the total energy, the transition is forbidden and, when a negative hopping probability is obtained (*e.g.*, due to the phase factor of $\rho_{lk}^{(I)}(t)$), the probability is set to zero. Upon a successful surface hop, the nuclear velocities are rescaled to satisfy the total energy conservation, and the running state is switched to the new state.

2.3 Computational details

All the quantum chemical computations are carried out using the beta-testing version of the TeraChem® program[31–36] (v1.92P, release 7f19a3bb8334), which implements the SSR method and the analytic derivatives formalism.[21] All the calculations employ the 6-31G* basis set[37] and the BH&HLYP exchange-correlation density functional.[38–40] The geometry optimizations are performed using the DL-FIND module[41] interfaced with TeraChem®. The geometries of the conical intersections are optimized by the CIOpt program[42] with the penalty function formalism and using the analytic energy gradients of the intersecting states.

The minimum energy pathways (MEPs) are obtained using the nudged elastic band (NEB) method with fixed end points.[41] The NEB method has an advantage that it converges to a MEP provided that sufficient number of discrete images are used.[43] For both the S_0 and S_1 states, the following MEPs were optimized: *E*P S_0min → CI_{90}, CI_{90} → *Z*P S_0min, *Z*P S_0min → CI_{270}, CI_{270} → *E*P S_0min; when joined, the MEPs complete a full loop of the motor. The *E*P S_0min → CI_{90} and *Z*P S_0min → CI_{270} legs of the total MEP comprise 40 discrete images, and the other two legs comprise 60 images.

The NAMD simulations are performed by the UNI-xMD program, a standalone code which implements the DISH-XF method.[22] When calculating the NAC vector, the gradients $\boldsymbol{\nabla} E_{S_k}$ ($k = 0, 1$) and $\boldsymbol{\nabla} \Delta_{SA}$ are calculated by the TeraChem® program and then picked up by an external script that implements Eq. (SI-3); the calculated NAC vectors, analytic gradients, and the S_1 and S_0 energies are parsed to the UNI-xMD code. The nuclear equations of motion are integrated using the velocity-Verlet algorithm with the time step of 20 a.u. (0.48 fs). The electronic equations of motion (SI-7) are integrated by the 4-th order Runge-Kutta method with the time step of 0.002 a.u. (4.8×10^{-5} fs). When integrating the electronic equations of motion, the electronic energies $E_l^{(I)}$ and the non-adiabatic $\sigma_{lk}^{(I)}$ couplings are linearly interpolated between the end points of the integration interval of the nuclear equations of motion.

The initial conditions at the start of the NAMD trajectories are set up by sampling the Wigner function of a canonical ensemble[44,45] at T = 300K. The trajectories starting in the *E*P conformation were propagated for 900 steps (432 fs) and the trajectories starting in the *Z*P conformation for 800 steps (384 fs). The trajectories were propagated using the NVE ensemble, *i.e.*, the microcanonical ensemble, where the total number of particles N, the system's volume V and the total – electronic + nuclear kinetic – energy E are conserved.

3 Cartesian coordinates of the S_0 and S_1 species and MECI points

Cartesian coordinates and total energies of the species reported in the main article.

Table SI-1: Cartesian coordinates (Å) and S_0 and S_1 total energies (hartree a.u.) of equilibrium conformations of DTPN obtained in SSR-BH&HLYP/6-31G* calculations.

	X	Y	Z	X	Y	Z
	*E*P conformation			*Z*P conformation		
C	2.334792	2.976554	-1.943717	2.352527	3.000545	-1.764580
C	1.044964	2.203749	-2.317369	1.114066	2.157455	-2.157003
C	0.629578	1.506197	-1.021541	0.644220	1.554939	-0.833508
H	2.118107	4.019790	-1.714566	2.074202	4.036743	-1.573466
H	3.066918	2.967571	-2.747637	3.113214	3.006247	-2.541731
H	0.263038	2.872648	-2.650732	0.339001	2.789363	-2.582774
C	-0.630422	1.172983	-0.718123	-0.650233	1.298891	-0.614639
C	1.306740	1.187917	-3.429295	1.486849	1.076612	-3.172501
H	2.077691	0.477781	-3.136425	2.300038	0.461655	-2.794795
C	-1.186759	0.621513	0.570233	-1.747604	1.424987	-1.647642
C	-2.684412	0.962346	0.504378	-2.933741	0.674654	-1.022515
N	-2.909432	1.117072	-0.912743	-2.613484	0.705818	0.382742
C	-1.784076	1.399104	-1.629411	-1.314318	0.984325	0.677103
O	-1.783125	1.754240	-2.788995	-0.859283	1.025527	1.797585
C	3.631114	0.997309	1.192900	3.622380	1.065182	1.405994
S	4.262978	2.206516	0.128896	4.256556	2.278463	0.344418
C	2.787693	2.237771	-0.732403	2.783803	2.304940	-0.519185
C	1.853132	1.395837	-0.212050	1.843431	1.472452	0.010760
C	2.353159	0.641597	0.913932	2.344731	0.707981	1.130569
H	4.259517	0.584906	1.960384	4.250776	0.655781	2.174793
H	0.396238	0.647907	-3.661930	0.646231	0.421527	-3.385877
H	1.639434	1.696427	-4.331878	1.807409	1.527903	-4.108839
C	1.662573	-0.461285	1.657473	1.660996	-0.408047	1.856412
H	1.193019	-1.162390	0.972242	1.177971	-1.084854	1.154481
H	2.379814	-1.014338	2.256374	2.387881	-0.980446	2.425833
H	0.891945	-0.093817	2.329239	0.889917	-0.039148	2.519400
H	-3.798322	1.368407	-1.299508	-3.245766	0.443738	1.112399
H	-3.305537	0.174433	0.919804	-3.883829	1.161377	-1.222490
H	-2.901030	1.883449	1.047150	-2.995640	-0.347730	-1.397024
H	-1.061568	-0.457821	0.627066	-2.014788	2.471124	-1.799482
H	-0.722774	1.054917	1.448730	-1.481530	1.015158	-2.616021
E(S_0)		-1032.177593			-1032.171758	
E(S_1)		-1031.995604			-1031.992806	

Table SI-2: Cartesian coordinates (Å), branching plane vectors (hartree/bohr) and total energies (hartree a.u.) of S_1/S_0 MECI points of DTPN obtained in SSR-BH&HLYP/6-31G* calculations.

	Cartesian coordinates			**g**-vector			**h**-vector		
	X	Y	Z	X	Y	Z	X	Y	Z
					CI_{90}				
C	2.646127	2.673245	-1.993325	0.039023	-0.028355	0.027922	-0.009491	-0.025583	-0.023771
C	1.159975	2.284831	-2.100157	-0.188993	0.082041	-0.007330	0.136347	-0.315333	-0.186139
C	0.831112	1.445071	-0.880733	0.297583	-0.189295	0.044822	-0.087985	-0.011323	-0.095616
H	2.811985	3.744242	-2.085444	-0.019742	0.003492	-0.017216	-0.025185	-0.006737	0.002737
H	3.244956	2.187027	-2.762005	-0.004119	-0.001741	-0.024673	0.022007	0.006649	0.005192
H	0.543556	3.167458	-1.892917	0.040050	0.037463	-0.087281	-0.010893	-0.027752	0.064473
C	-0.455480	0.961685	-0.543459	0.087461	-0.043013	-0.396858	0.043554	-0.098957	0.075574
C	0.739594	1.703835	-3.443199	0.042866	0.020940	0.012290	0.002828	0.042466	-0.044478
H	1.272227	0.780175	-3.657669	0.000451	-0.004422	0.002456	-0.001795	0.009725	0.005763
C	-1.196591	-0.210466	-1.155493	-0.056354	-0.024351	0.159747	-0.052668	0.197111	-0.356124
C	-2.553946	-0.048712	-0.458869	-0.049448	-0.082456	-0.032528	0.000915	0.032940	0.028576
N	-2.691879	1.385783	-0.359433	0.150148	0.053018	0.089111	-0.046287	-0.015046	-0.127527
C	-1.405556	1.960308	-0.207359	-0.497342	0.311435	0.224664	0.134757	-0.184624	0.573372
O	-1.247320	3.135884	0.116135	0.044988	-0.273966	-0.069403	-0.012845	0.051788	-0.079164
C	3.569208	1.267315	1.570497	0.070338	0.043666	-0.020644	-0.014859	-0.003784	-0.000281
S	4.359779	2.239588	0.340504	0.105067	-0.033848	0.121163	0.023228	-0.026405	-0.020231
C	3.000340	2.154750	-0.649295	-0.138347	-0.075345	0.065405	-0.000486	-0.018869	0.003663
C	1.976069	1.431875	-0.057960	0.055996	0.062893	-0.007144	-0.117015	0.396982	0.187542
C	2.315843	0.896030	1.240628	0.020122	0.045555	-0.063880	0.010654	0.007452	-0.006654
H	4.111845	1.034744	2.468068	-0.001269	-0.003092	0.004325	0.001421	-0.002762	-0.001787
H	-0.323958	1.499692	-3.453592	-0.013744	-0.000524	-0.021018	0.000119	-0.001002	0.001949
H	0.961075	2.410309	-4.239347	-0.006736	-0.001837	-0.012292	-0.007112	-0.001008	-0.013627
C	1.427471	0.021547	2.062774	0.029691	-0.006210	-0.041955	-0.027450	0.002343	0.007917
H	1.454539	-0.996781	1.678998	-0.001956	-0.013608	0.008518	0.005240	-0.001342	-0.003772
H	1.749066	0.001823	3.099130	-0.024965	-0.000257	0.002786	-0.002027	0.001810	-0.001667
H	0.400751	0.358847	1.990856	-0.018011	0.003824	0.040510	0.015610	-0.009155	0.015008
H	-3.362932	1.746133	0.296874	-0.032067	0.021269	-0.041720	0.021749	0.017648	-0.014036
H	-3.365842	-0.493499	-1.029695	-0.001010	0.008996	0.015235	0.005283	-0.003591	0.007010
H	-2.519332	-0.532346	0.521802	-0.016109	0.002296	-0.010514	0.003951	-0.000845	0.003881
H	-1.335749	-0.162826	-2.242009	0.057207	0.055029	0.040310	-0.045386	-0.061533	-0.028297
H	-0.760936	-1.184374	-0.935902	0.029221	0.030402	-0.004808	0.033819	0.048736	0.020515
$E(S_0)$		-1032.061857							
$E(S_1)$		-1032.061842							
					CI_{270}				
C	2.635393	2.986506	-1.725426	0.002467	0.025942	0.051067	0.019576	-0.011552	0.014522
C	1.224313	2.459384	-2.066171	-0.094587	-0.092438	-0.087797	0.059795	-0.316739	-0.159356
C	0.721985	1.745177	-0.830760	0.185692	0.138061	-0.098043	-0.018927	0.028113	0.081512
H	2.631450	4.066484	-1.585989	-0.001737	0.012632	-0.012370	-0.019094	-0.003444	-0.004861
H	3.377371	2.767486	-2.487843	-0.015811	-0.001854	-0.026076	0.014069	0.008807	0.001944
H	0.527285	3.261783	-2.297075	0.028598	0.038846	-0.035567	0.012703	-0.026046	0.050174
C	-0.608754	1.307054	-0.669048	0.148200	0.242953	0.375692	-0.055716	0.058036	-0.046927
C	1.209035	1.460687	-3.236535	0.031530	0.072066	0.001571	0.011700	0.024695	-0.040626
H	1.970085	0.697017	-3.099788	-0.003421	-0.001150	0.004300	-0.000538	0.008198	0.003444
C	-1.565079	1.977136	0.300340	-0.134966	-0.066419	-0.106643	0.225501	-0.179996	0.335927
C	-2.754813	1.011829	0.207624	-0.069823	0.059548	0.072260	-0.001866	-0.033107	-0.027318
N	-2.121158	-0.267109	-0.015000	0.110052	0.046886	-0.153925	0.009831	0.019710	0.119725
C	-0.917497	-0.068820	-0.732055	-0.267444	-0.588589	-0.082923	-0.178781	0.095479	-0.561203

Continued on next page

Table SI-2 – *Continued from previous page*

	Cartesian coordinates			**g**-vector			**h**-vector		
	X	Y	Z	X	Y	Z	X	Y	Z
O	-0.303646	-1.003660	-1.245903	-0.085887	0.258529	0.078217	0.007828	-0.048050	0.061728
C	3.356996	1.053071	1.638754	0.069129	0.036810	-0.012235	-0.005927	0.007689	0.002722
S	4.259627	2.100275	0.554657	0.092968	-0.053879	0.113707	0.014213	-0.035062	-0.028443
C	2.914530	2.283759	-0.444714	-0.142422	-0.074798	0.034267	0.013954	-0.021808	-0.011921
C	1.817935	1.593433	0.044914	0.033581	0.028246	0.010384	-0.114001	0.437167	0.227506
C	2.078533	0.856008	1.258467	0.025495	0.047584	-0.053442	-0.003317	-0.015840	-0.008088
H	3.865323	0.628342	2.484414	-0.002518	-0.002257	0.004587	0.000889	-0.003181	-0.003273
H	0.246467	0.965379	-3.287256	0.000527	-0.009410	-0.028671	-0.006857	-0.004770	-0.003013
H	1.399738	1.983922	-4.169861	-0.000499	-0.014881	-0.028295	-0.008850	-0.013815	-0.012945
C	1.103144	-0.061442	1.917810	0.014180	0.007563	-0.015558	-0.002749	0.004764	0.002176
H	0.791024	-0.825010	1.209710	0.008097	-0.014678	0.020373	-0.000567	0.006715	-0.000845
H	1.546521	-0.535937	2.787325	-0.013307	-0.006035	0.000997	0.000269	-0.000036	-0.000361
H	0.207319	0.467840	2.227505	-0.006707	-0.002301	0.022616	-0.003197	0.001408	0.006202
H	-2.687123	-1.007106	-0.392281	0.008073	-0.030763	0.045279	0.032007	-0.004128	0.002641
H	-3.356650	1.008476	1.113611	-0.003485	-0.013329	-0.015111	-0.002251	0.004424	-0.008446
H	-3.390332	1.311574	-0.629266	-0.008335	-0.011240	0.013002	0.001155	0.003024	-0.001955
H	-1.198230	2.033451	1.334416	0.051563	-0.021351	-0.076282	-0.048692	0.031728	0.052816
H	-1.866500	2.985997	0.018727	0.040798	-0.010294	-0.015382	0.047840	-0.022380	-0.043457
E(S_0)		-1032.063607							
E(S_1)		-1032.063592							

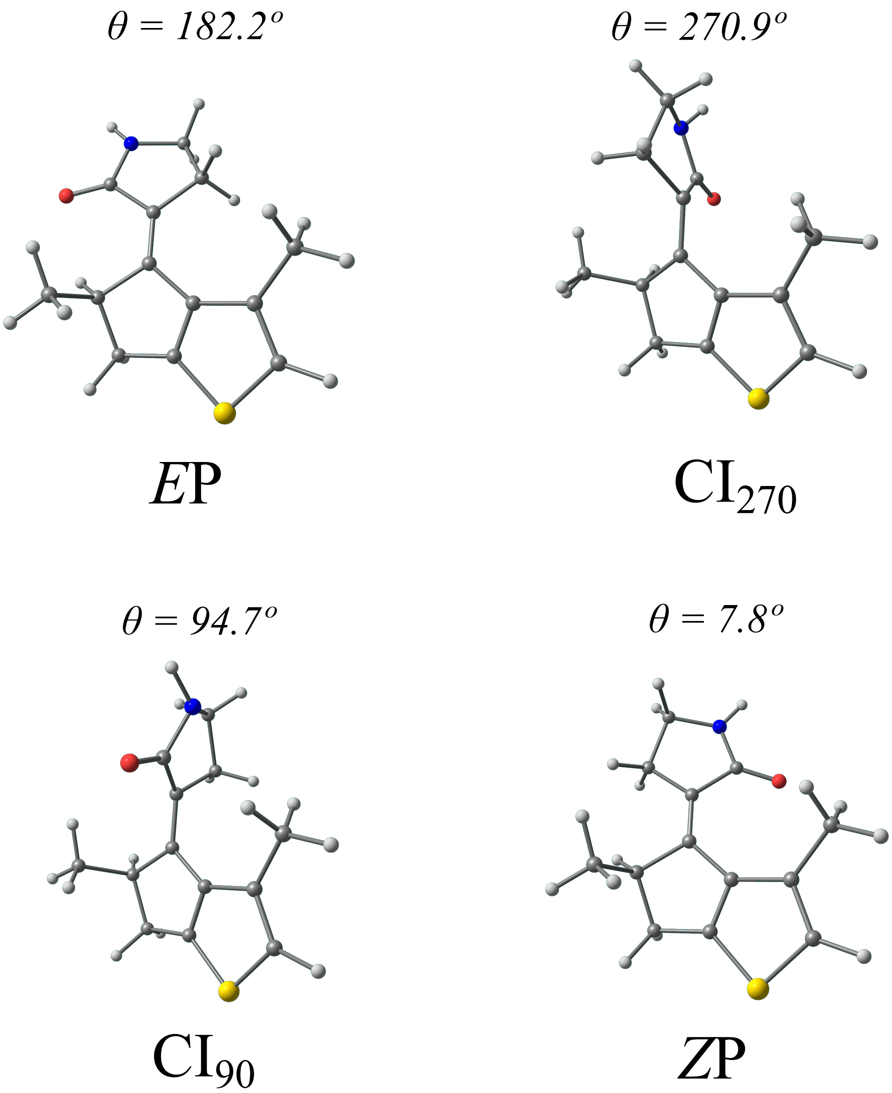

Figure SI-1: Molecular geometries of the ground state minima and conical intersections of DTPM. For definition of the central dihedral angle θ, see Scheme 2 of the main text.

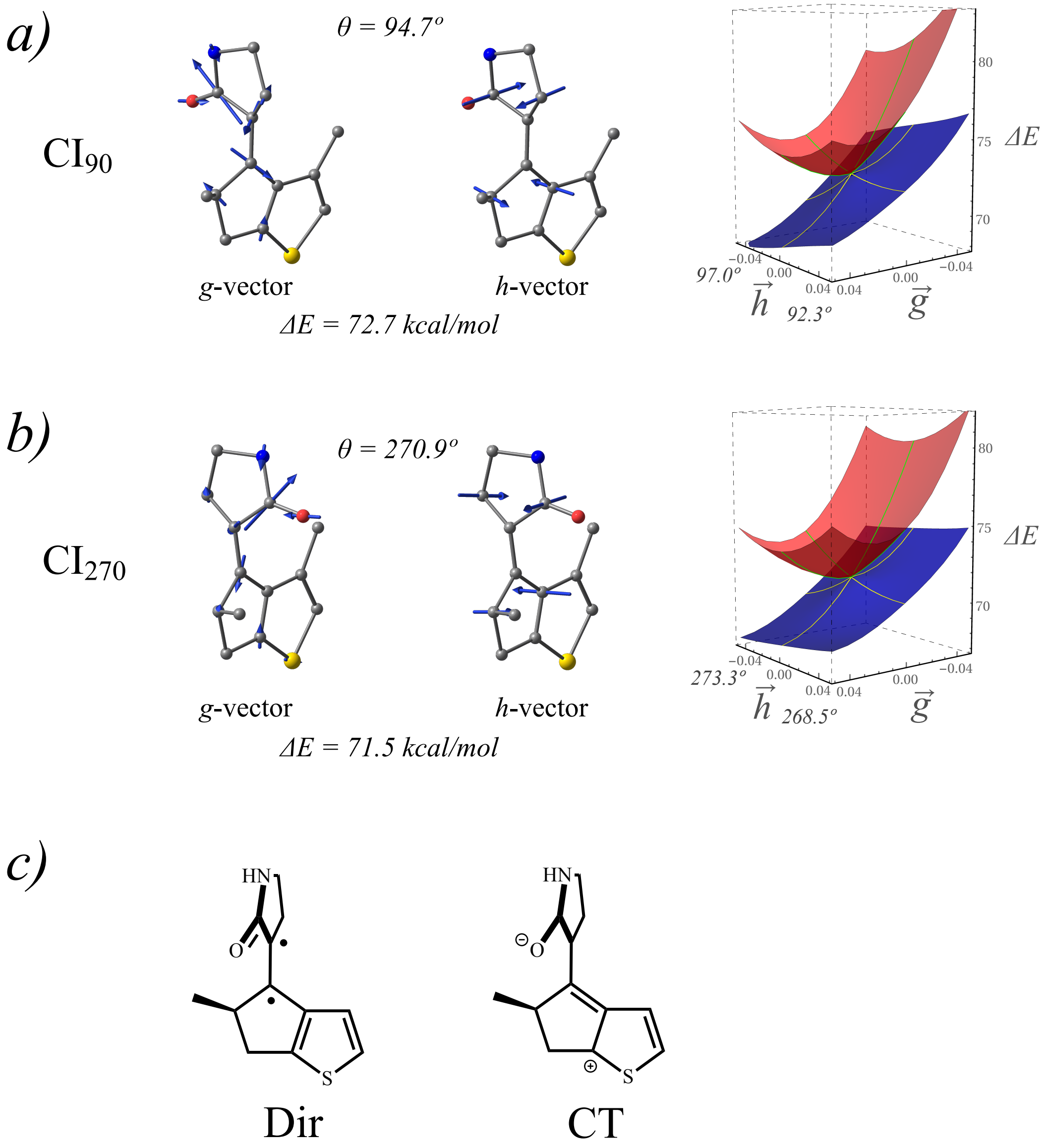

Figure SI-2: The branching plane (BP) vectors of the S_1/S_0 conical intersections CI_{90} and CI_{270} (obtained by torsion about the C_4=$C_{3'}$ bond through *ca.* 90° and 270°, respectively) of the DTPN motor optimized in this work. Panels a) and b) show the geometries and the branching plane vectors $\vec{g}$ and $\vec{h}$ of the CIs (hydrogen atoms removed for clarity). The relative energies ΔE (in kcal/mol) are given with respect to the **2**(*E*P) ground state energy. See Scheme 2 of the main text for definition of the dihedral angle θ. The scans of the S_1 (red) and S_0 (blue) PESs near the respective CIs are shown on the right hand side of the respective panels. Panel c) shows the Lewis structures of the ground and excited electronic states at a CI geometry.

4 Vertical excitation energies and absorption spectra of *E*P and *Z*P conformations

At the S_0 equilibrium geometries of *E*P and *Z*P (optimized by the SSR-BH&HLYP/6-31G* method), the vertical excitation energies (VEEs) were calculated by both the SSR method and the TD-DFT method with the same density functional and basis set, *i.e.*, TD-BH&HLYP/6-31G*. Table SI-3 compares the excitation energies obtained in both sets of calculations. There is a good agreement between the VEEs obtained by both methods for the optically bright S_1 state; the latter state corresponds to a $\pi \rightarrow \pi^*$ one-electron transition centered around the $C_{3'}$=C_4 double bond and has a large oscillator strength. The S_2 and S_3 states have charge transfer character and involve transitions from the lone pair orbitals of the O atom (S_2) and the S atom (S_3) to the π^* orbital of the $C_{3'}$=C_4 bond. These excited states lie *ca.* 0.2–0.4 eV above the S_1 state and have a very low oscillator strengths. The S_4 state corresponds to a one-electron transition from the doubly occupied π orbital of the $C_{3'}$=C_4 bond to the anti-bonding π^* orbital of the C_{3a}=C_{6a} bond; this state has a modest oscillator strength and lies *ca.* 0.9–1.0 eV above the S_1 state. Hence, the S_1 state is an optically bright state populated by the photoexcitation and a photochemically active state leading to breaking the π component of the central $C_{3'}$=C_4 double bond.

Table SI-3: Vertical excitation energies (eV) of the ground state equilibrium conformations of DTPN motor obtained in the SSR-BH&HLYP/6-31G* and TD-BH&HLYP/6-31G* calculations. Oscillator strengths of the transitions are given in parentheses.

	SSR	TD-DFT			
conformation	$S_1 \leftarrow S_0$	$S_1 \leftarrow S_0$	$S_2 \leftarrow S_0$	$S_3 \leftarrow S_0$	$S_4 \leftarrow S_0$
*E*P	4.95 (0.39)	4.96 (0.49)	5.16 (0.00)	5.60 (0.04)	5.80 (0.24)
*Z*P	4.87 (0.35)	4.84 (0.40)	5.23 (0.01)	5.41 (0.16)	5.82 (0.15)

The UV absorption spectra of the *E*P and *Z*P conformers were simulated theoretically[46] by convolution of the vertical excitations calculated at one hundred geometries obtained from sampling the Wigner function of the respective conformer at T=300K. The Lorentzian lineshape $L(\lambda; \lambda_i, f_{\lambda_i}) = f_{\lambda_i} \frac{\sigma^2}{\sigma^2+(\lambda-\lambda_i)}$, centered around the calculated excitation wavelengths λ_i with an amplitude given by the respective oscillator strength f_{λ_i} and broadened by a uniform width σ = 10 nm was used to simulate absorption spectra of the lowest (S_1) absorption band. The resulting spectra are shown in Fig. SI-3. SSR and TD-DFT predict very close absorption maxima for the $S_1 \leftarrow S_0$ transition; 264 nm (SSR) and 268 nm (TD-DFT) for the *E*P conformation and 268 nm (SSR) and 273 nm (TD-DFT) for the *Z*P conformation. However, the shapes of the lowest absorption band of the *E*P and *Z*P conformers are somewhat different. The lower left panel of Fig. SI-3 shows the difference of the calculated absorptivities of the *E*P and *Z*P conformations. At 299 nm, the *E*P conformer shows noticeably lower absorptivity than *Z*P; the latter is much less absorbing at 263 nm. The lower right panel shows the ratio of the *E*P and *Z*P absorptivities. The *Z*P conformer has *ca.* 1.4 times lower absorptivity than the *E*P conformer at 235 nm. The ratio is inverted (to *ca.* 0.7) at the wavelength of 311 nm. The described differences in the absorptivity of the *E*P and *Z*P conformers can be used for their identification during the photoreactions and for manipulating the course of the photoreactions by predominantly exciting one of the conformers.

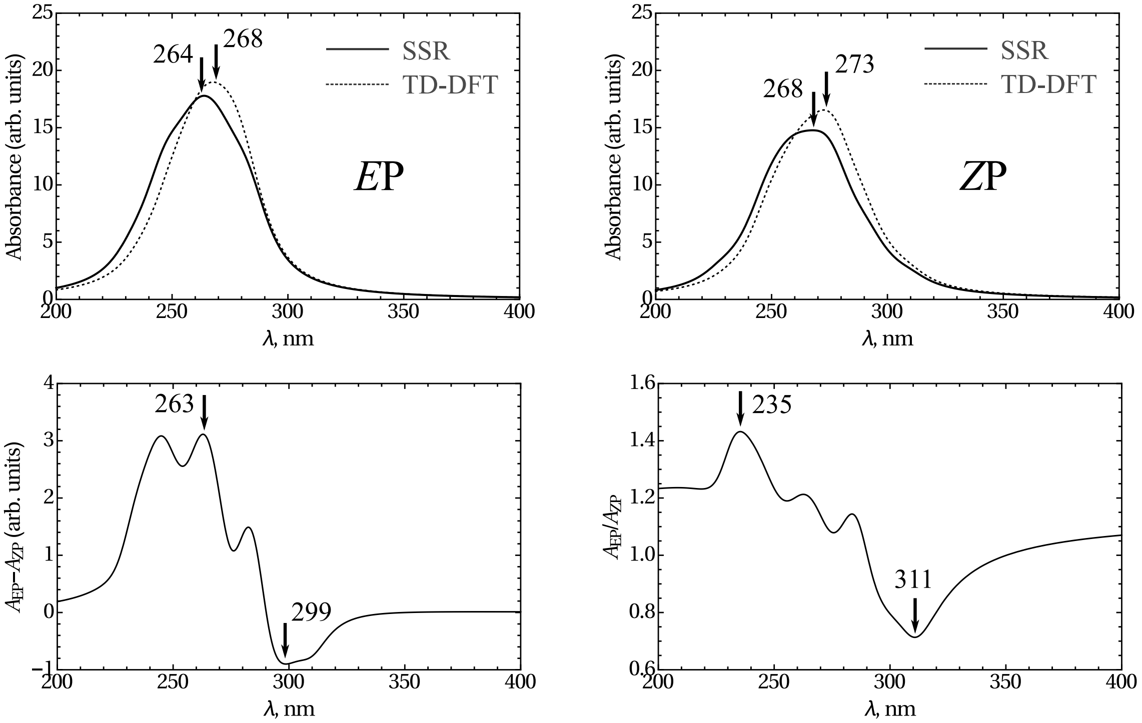

Figure SI-3: First excitation band of the DTPN motor calculated by the SSR-BH&HLYP/6-31G* (solid line) and by TD-BH&HLYP/6-31G* (dashed line) methods. Difference of the absorbances and ratio of the absorbances are shown in the lower left and right panels, respectively.

5 Total charges on the pyrrolidinone blade of DTPN along the S_1 and S_0 MEPs

The total charges on the pyrrolidinone blade along the MEPs, see Figure SI-4, were calculated by summing up the Mulliken charges on the respective atoms. The Mulliken charges were calculated from the relaxed SSR density matrices[21] of the S_1 and S_0 states. The relaxed density matrices calculated by the TeraChem® program were saved in the form of the natural orbitals and orbital occupation numbers to an external file in the "molden" format. The SSR natural orbitals were used by the OrbKit suite[47] to obtain the Mulliken charges.

At the FC geometry, the photoexcitation is due to a one-electron $\pi \rightarrow \pi^*$ transition located around the $C_{3'}{=}C_4$ bond (axle of the motor); which breaks the π component of the bond. Near the FC points, the pyrrolidinone total charge Q varies in the range of -0.1–-0.2, which indicates that both states, S_1 and S_0, possess covalent character. On the S_0 MEP, the pyrrolidinone's charge remains small, *ca.* -0.1–-0.2, whereas the pyrrolidinone's charge along the S_1 MEP rapidly decreases towards CIs. This indicates that breaking of the π component of the $C_{3'}{=}C_4$ double bond occurs by homolytic (diradical) mechanism in the S_0 state and that the S_1 state has predominantly charge transfer character. At the CIs, where the S_1 and S_0 energies become degenerate, the S_0 state remains covalent ($Q \sim -0.1$–-0.2) and the S_1 state has a pronounced ionic character ($Q \sim -0.5$).

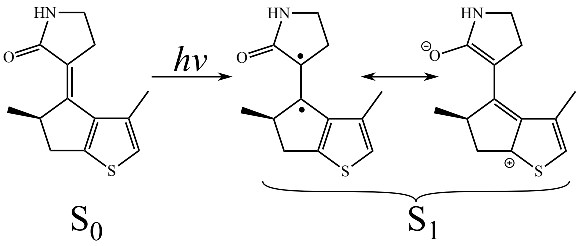

6 Results of NAMD simulations

For each of the equilibrium S_0 conformations, *E*P and *Z*P, one hundred initial conditions were generated by sampling the Wigner function of the respective conformation at T = 300K. Out of one hundred initial conditions, 36 were randomly selected to run the trajectories. Starting in the S_1 state at the initial geometries and with the initial nuclear velocities, 36 *E*P trajectories were propagated for 432 fs (900 steps; integration step 0.48 fs) and 36 *Z*P trajectories were propagated for 384 fs (800 steps). All the trajectories underwent transition to the S_0 state within the allotted time.

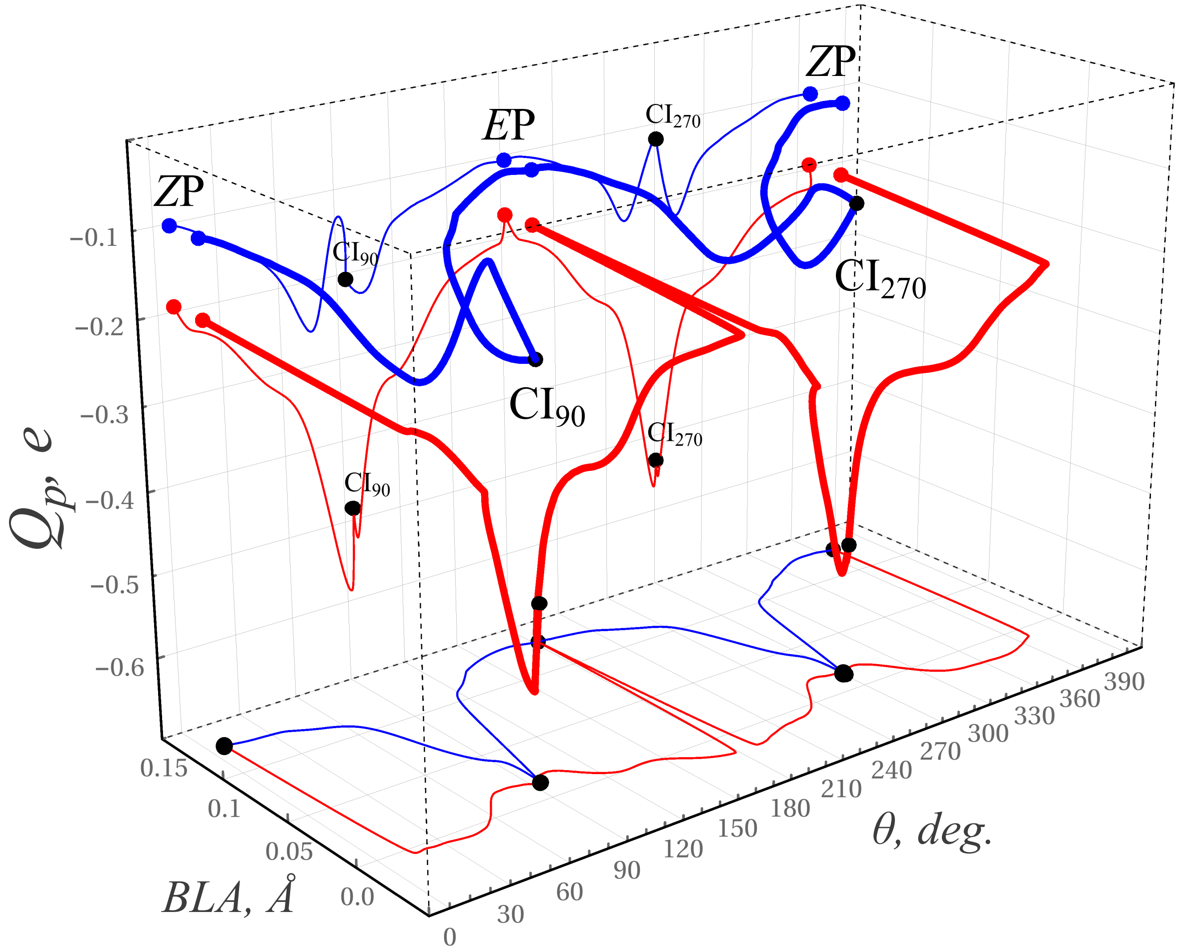

Figure SI-4: Total charge Q pyrrolidinone blade of DTPN along the S_1 (red) and S_0 (blue) MEPs as a function of the dihedral angle θ (see Scheme 2 of the main text for definition) and the BLA distortion.

The trajectories were analyzed visually and the distribution of the products was obtained from the distribution of the dihedral angle θ, for definition see Scheme 2 of the main article. The distributions of the dihedral angle θ at the start and at the end of the *E*P and *Z*P trajectories are shown in Figure SI-5 and the variations of the dihedral angle θ with the propagation time are shown in Fig. SI-6.

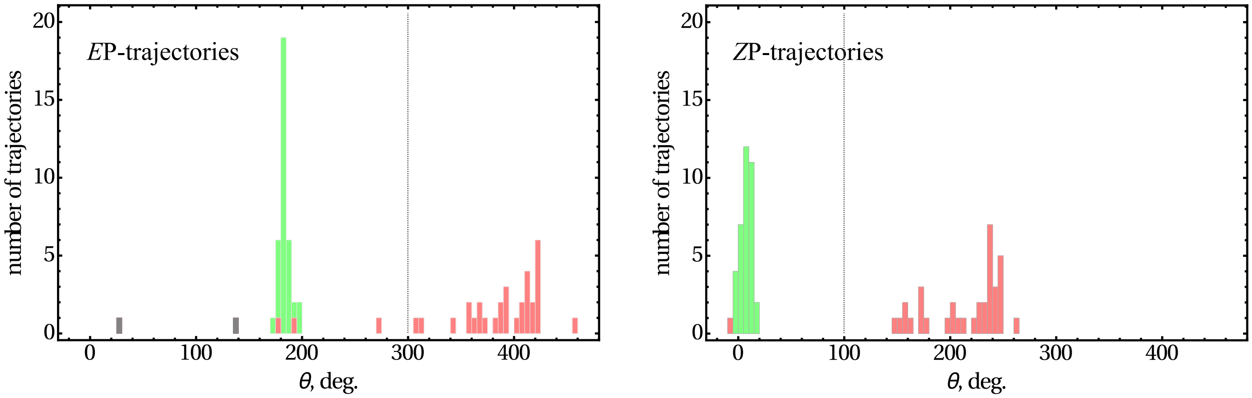

Figure SI-5: Distribution of the dihedral angle θ (in deg.) at the start of the trajectories (green) and at the end of the trajectories (red). Grey bars in the left panel show the θ values at the end of the renegade *E*P-trajectories propagating in the opposite (*i.e.*, CW) direction. Vertical dotted lines show the cut-off θ value used to discriminate between the reactants (to the left of the line) and products (to the right of the line).

At the end of the *E*P trajectories, 3 trajectories fell back (N^{EP}_{back}) to the *E*P conformation and 31 (N^{EP}_{fwrd}) continued to the *Z*P conformation; the quantum yield of isomerization is calculated as $\phi_{\mathrm{EP}\to\mathrm{ZM}} = \frac{N^{EP}_{fwrd}}{N^{EP}_{fwrd}+N^{EP}_{back}}$, which yields the value reported in Table 2 of the main article, 0.91 ± 0.05. The latter value and its statistical uncertainty were obtained by the bootstrap resampling[48] of the distribution of the dihedral angle θ at the end of the trajectories. When deciding which trajectory yields the *Z*P or the *E*P conformation, a threshold value $\theta_{thrsh} = 300^\circ$ was used; ZP corresponds to $\theta > \theta_{thrsh}$ and *E*P to $\theta \leq \theta_{thrsh}$.

A similar procedure was applied to the analysis of the *Z*P trajectories. Out of the 36 ZP trajectories 1 returned back to ZP and 35 moved forward to *E*P; the $\phi_{\mathrm{ZP}\to EM}$ quantum yield with the margin of error estimated by bootstrapping is 0.97 ± 0.03, see Table 2 of the main article. The threshold value of θ used to discriminate between *E*P and *Z*P was set at 100°, see Fig. SI-5.

All 36 *Z*P trajectories followed torsion of the pyrrolidinone unit in the counterclockwise (CCW) direction. From the 36 *E*P trajectories 34 followed torsion in the CCW direction and 2 in the CW direction. The two renegade trajectories were discarded when determining the quantum yield and the S_1 lifetime of the *E*P trajectories. The origin of the imperfect directionality of the *E*P trajectories is discussed later. Here, it is described how the unidirectionality of the torsion was determined for the *E*P and *Z*P trajectories.

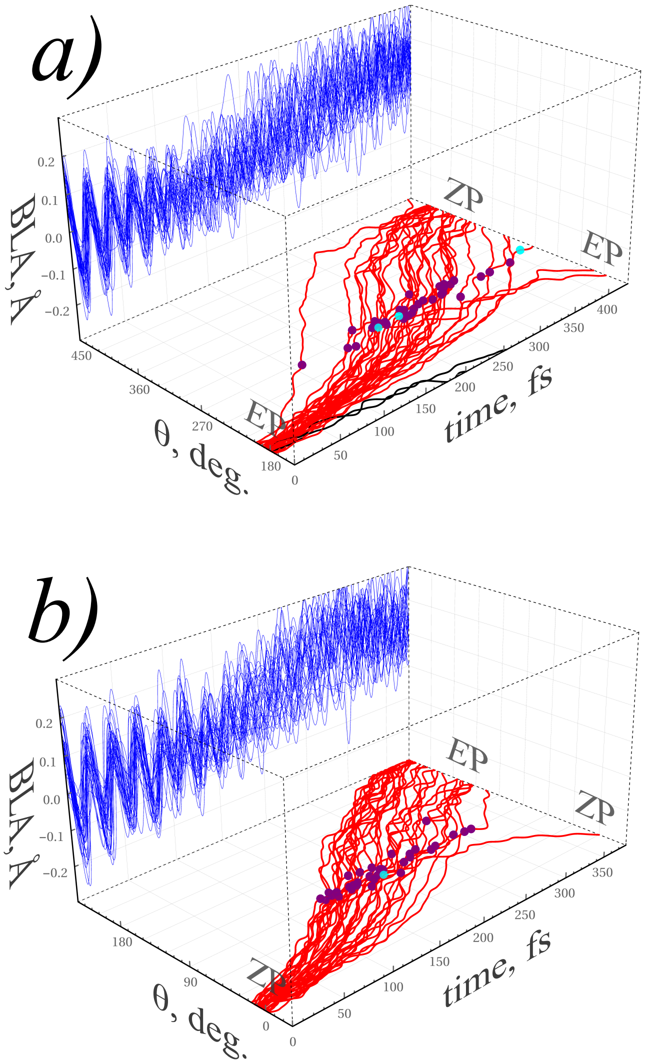

Figure SI-6: Dihedral angle θ (deg.) and the BLA distortion (Å) as functions of the propagation time (fs) along the NAMD trajectories initiated in the *E*P conformation (a) and in the *Z*P conformation (b). Purple dots show the $S_1 \rightarrow S_0$ surface hops for the trajectories propagating in the direction of isomerization (to the *Z*P and *E*P conformations, respectively) and cyan dots show the surface hops for the trajectories turning back to the initial conformation. The black curves in the panel a) show the two renegade trajectories propagating in the opposite (*i.e.*, CW) direction of torsion.

The unidirectionality *uni* is defined as the ratio $\frac{N^{CCW}}{N^{CCW}+N^{CW}}$ of the number of trajectories N^{CCW} undergoing torsion in the CCW direction to the total number of trajectories $N^{CCW} + N^{CW}$. Obviously, the *Z*P trajectories display perfect 100% unidirectionality, see Table 2 of the main article. For the *E*P trajectories, the CCW and CW trajectories were discriminated by the angle θ at the time of the $S_1 \to S_0$ surface hop, see Fig. SI-6, where the hop events are shown as purple (for forward trajectories) or cyan (for backward trajectories) dots. Most of the hops, for the CCW propagating trajectories, occur near $\theta \sim 270°$ (*i.e.*, near CI_{270}) and, for the CW propagating trajectories, near $\theta \sim 90°$ (CI_{90}). Hence, the value of θ^{hop} can be used to discriminate between CCW and CW trajectories, *e.g.*, setting $\theta_{thrsh}^{CCW/CW} = 180°$. The value of the unidirectionality $uni = 0.94 \pm 0.04$ reported in Table 2 of the main article was obtained from the distribution of the θ^{hop} values for the *E*P trajectories as $\frac{N^{CCW}}{N^{CCW}+N^{CW}}$ and its margin of error determined by bootstrapping (with 10^4 samples).

The distribution of the $S_1 \to S_0$ hop times for the *E*P and *Z*P trajectories is shown in Fig. SI-7. The hop times were fitted by a Gaussian distribution $g(t) = \frac{1}{\sigma\sqrt{2\pi}} e^{-\frac{(t-\mu)^2}{2\sigma^2}}$ with the mean μ and dispersion σ. The values of μ and σ reported in Table 2 of the main article were obtained by the bootstrap method with 10^4 samples. These values are reported in Table 2 of the main article and used in the Gaussian curves shown in Fig. SI-7.

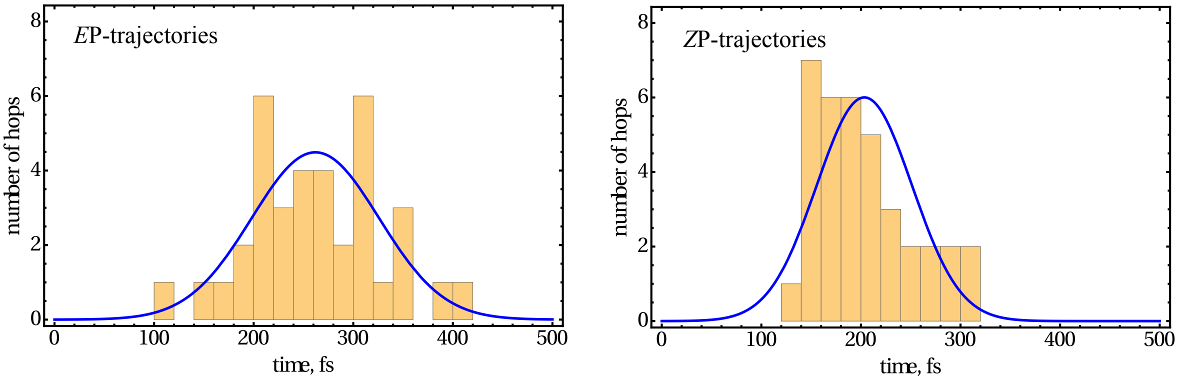

Figure SI-7: Distribution of hop times for the *E*P (left panel) and *Z*P (right panel) trajectories. Blue curves show probability density of the the hop times fitted using the normal distribution, see Table 2 for the fitted values of the mean (μ) and standard deviation (σ) of the normal distribution.

Population of the S_1 state as a function of propagation time was calculated as a fraction of all the trajectories residing in the S_1 state at a given instance t. The S_1 populations $n_{S_1}(t)$ obtained from the raw data for the *E*P and *Z*P trajectories are shown in Fig. SI-8 by blue dots. The raw populations were fitted by an exponential function $f(t) = e^{-\frac{t-t_0}{\tau}}$ with the offset t_0 and the exponential decay parameter τ. The populations $n_{S_1}(t)$ were resampled by bootstrapping and, for each bootstrap image, the exponential fit was repeated. The values of the offset t_0 and the decay constant τ shown in Table 2 were then obtained by averaging over all the bootstrap samples. For all the bootstrap samples, the value of the R^2 parameter was calculated and then averaged over all the samples. The averaged R^2 for the *E*P and *Z*P trajectories are 0.966 ± 0.015 and 0.992 ± 0.004, respectively. The exponential fit curves with the bootstrapped parameters t_0 and τ are shown in Fig. SI-8 in red color. The S_1 lifetimes were obtained for each bootstrap sample as $\tau_{S_1} = t_0 + \tau^*$ and then averaged over all the samples. The final S_1 lifetime values are reported in Table 2 of the main article.

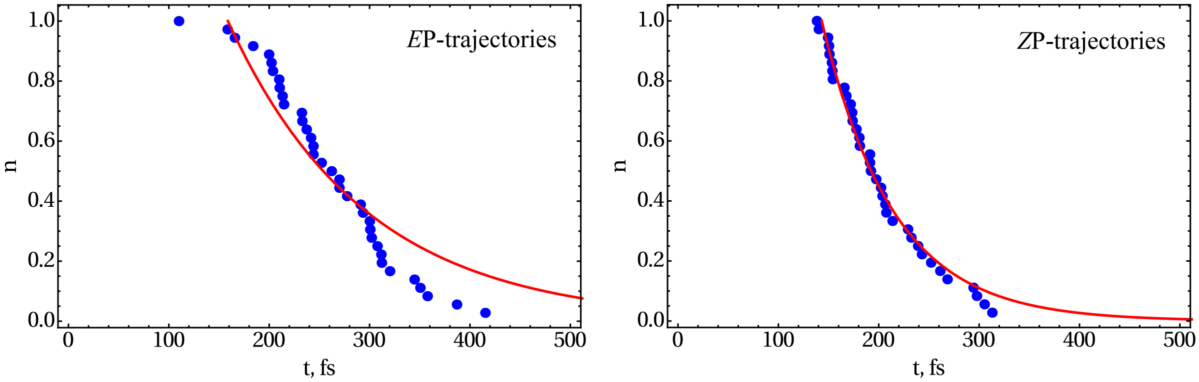

Figure SI-8: Population (n) of the S_1 state as a function of the propagation time t (in fs). The S_1 populations are shown by blue dots and the exponential fits are shown by the red curves. See Table 2 for the parameters of the exponential decay.

For the two renegade *E*P trajectories undergoing torsion in the CW, rather than CCW, direction, the initial geometries (generated by sampling the Wigner function) were inspected. As the Wigner function is build upon the normal modes of the S_0 equilibrium geometry of *E*P, the amplitudes $a_k(i)$ of the normal modes $\mathbf{Q}_k$ in the generated initial geometries $\mathbf{R}(i)$ were calculated

$$a_k(i) = \mathbf{Q}_k^\dagger \cdot (\mathbf{R}(i) - \mathbf{R}_0)\,, \tag{SI-10}$$

where i labels the initial geometry and $\mathbf{R}_0$ is the equilibrium geometry of *E*P. Then, the amplitudes $a_k(i)$ were averaged over all (N_{traj}) the initial conditions $\bar{a}_k = \frac{1}{N_{traj}} \sum_{i=1}^{N_{traj}} a_k(i)$. The average amplitudes $\bar{a}_k$ of the low frequency modes of *E*P are shown in the right panel of Fig. SI-9 for the CCW trajectories (blue, $N_{traj} = 34$) and the CW trajectories (red,

---

[*] This follows from the condition $f(\tau_{S_1}) = e^{-1}$

$N_{traj} = 2$). The amplitudes of the higher frequency modes average out to near zero values (as it ought to be). To inspect the absolute magnitude of the displacements along the normal modes to the initial geometries the square amplitudes $a_k^2(i)$ were also calculated and averaged over the CCW and CW trajectories. The average square amplitudes $\bar{a}_k^2$ are shown in the left panel of Fig. SI-9.

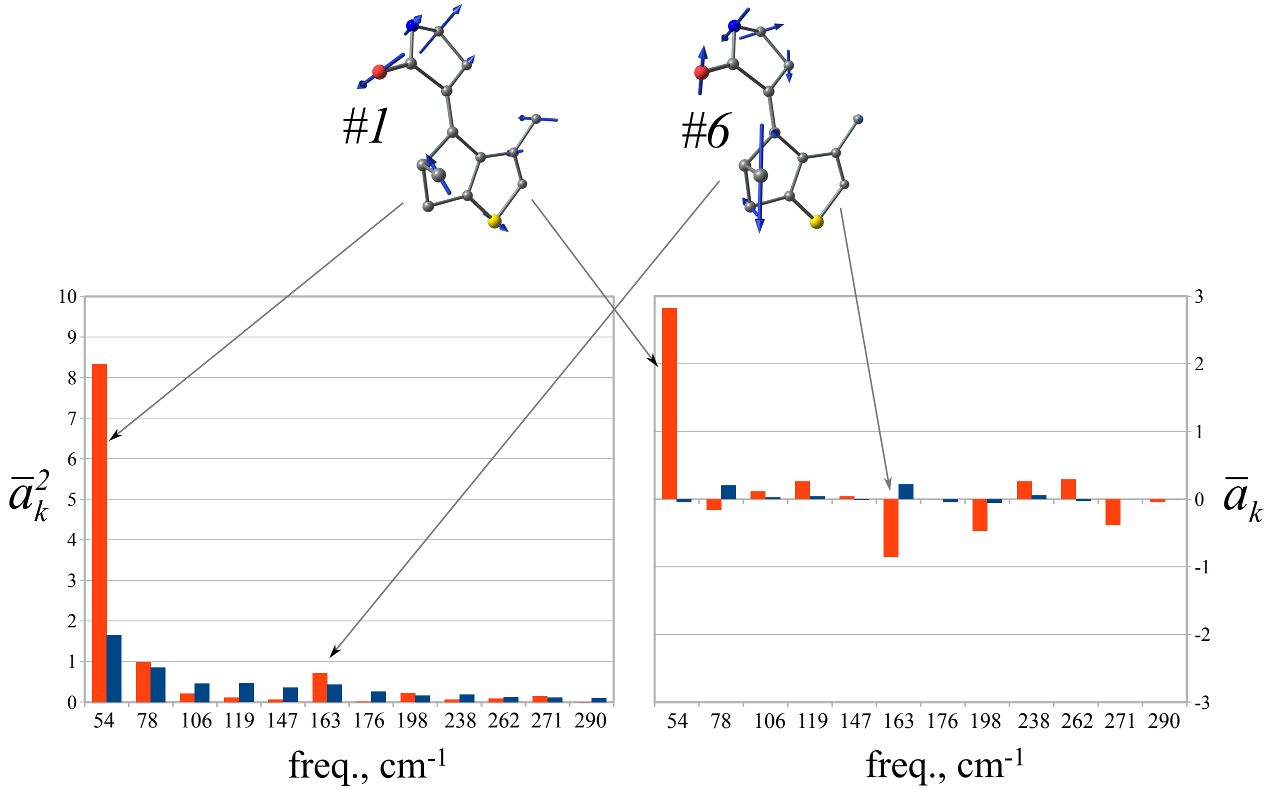

Figure SI-9: Average squares $\bar{a}_k^2$ of the amplitudes of the normal modes (left panel) and average amplitudes $\bar{a}_k$ of the normal modes (right panel) for the initial geometries of the *E*P trajectories. Red columns show amplitudes for the CW trajectories, blue columns for the CCW trajectories. The two normal modes whose contributions into the CW trajectories stand out are shown in the upper panel.

From Fig. SI-9 it is obvious that two normal modes make conspicuously large contributions to the initial geometries of the CW propagating trajectories. These are the lowest frequency mode $\mathbf{Q}_1$ and the mode $\mathbf{Q}_6$. The former corresponds predominantly to a tilting motion of the pyrrolidinone blade, the latter to puckering of the pyrrolidinone ring. Large amplitudes of these modes result in a geometry where the pyrrolidinone ring attains flatter (less puckered) shape and a noticeably more upright orientation than in the S_0 equilibrium geometry of *E*P.

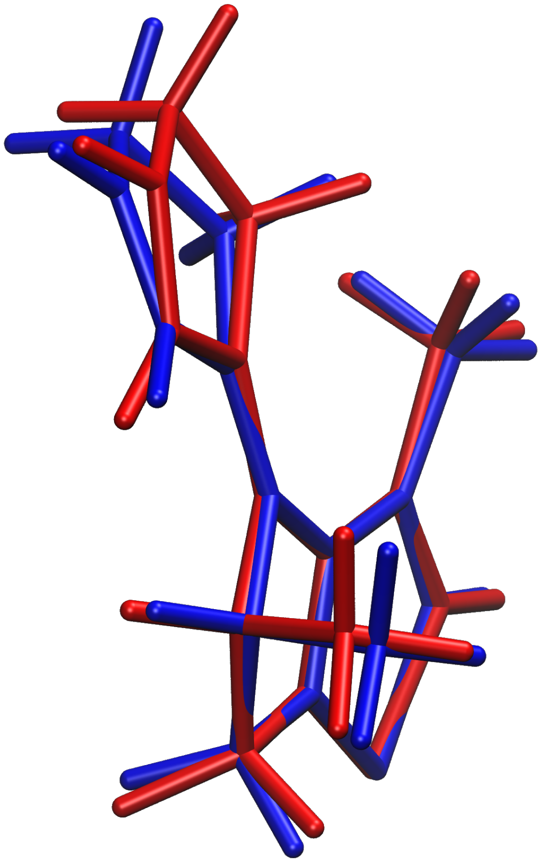

Figure SI-10: Superimposed initial geometries of the trajectories propagating in the direction of the CCW torsion (blue) and the CW torsion (red). The initial geometries are averaged over all the respective trajectories.

In Fig. SI-10, the initial geometries of the CCW and CW trajectories averaged over all the respective trajectories are shown in blue (CCW) and red (CW) color. The geometric difference results in a certain degree of pre-twist of the CW initial geometries which favors propagation in the wrong direction. The vary large amplitudes of the modes $\mathbf{Q}_1$ and $\mathbf{Q}_6$ became possible due to sampling the Wigner function at the ambient temperature, when it may be expected that many low frequency modes are excited. At lower temperatures, large displacements along these modes are less likely to occur. Hence, the unidirectionality of the *E*P trajectories should improve at lower temperatures. However, even though the initial conditions of the current NAMD simulations were, perhaps, the least favorable, a sufficiently high unidirectionality, *ca.* 94%, was obtained in the simulations, see Table 2 of the main article.

References

(1) Paolino, M.; Gueye, M.; Pieri, E.; Manathunga, M.; Fusi, S.; Cappelli, A.; Latterini, L.; Pannacci, D.; Filatov, M.; Léonard, J.; Olivucci, M. Design, Synthesis, and Dynamics of a Green Fluorescent Protein Fluorophore Mimic with an Ultrafast Switching Function. *J. Am. Chem. Soc.* **2016**, *138*, 9807–9825.

(2) Pinna, G.; Curzu, M. M.; Dore, A.; Lazzari, P.; Ruiu, S.; Pau, A.; Murineddu, G.; Pinna, G. A. Tricyclic pyrazoles part 7. Discovery of potent and selective dihydrothienocyclopentapyrazole derived CB2 ligands. *Eur. J. Med. Chem.* **2014**, *85*, 747–757.

(3) Ewen, J. A.; Elder, M. J.; Jones, R. L. Patent No.: US 6,635,779 Date of Patent: Oct. 21, 2003.

(4) Landaluce, T. F.; London, G.; Pollard, M. M.; Rudolf, P.; Feringa, B. L. Rotary Molecular Motors: A Large Increase in Speed through a Small Change in Design. *J. Org. Chem.* **2010**, *75*, 5323–5325.

(5) Filatov, M.; Shaik, S. A spin-restricted ensemble-referenced Kohn-Sham method and its application to diradicaloid situations. *Chem. Phys. Lett.* **1999**, *304*, 429–437.

(6) Moreira, I. d. P. R.; Costa, R.; Filatov, M.; Illas, F. Restricted ensemble-referenced Kohn-Sham versus broken symmetry approaches in density functional theory: Magnetic coupling in Cu binuclear complexes. *J. Chem. Theory Comput.* **2007**, *3*, 764–774.

(7) Kazaryan, A.; Heuver, J.; Filatov, M. Excitation Energies from Spin-Restricted Ensemble-Referenced Kohn-Sham Method: A State-Average Approach. *J. Phys. Chem. A* **2008**, *112*, 12980–12988.

(8) Filatov, M. Assessment of density functional methods for obtaining geometries at conical intersections in organic molecules. *J. Chem. Theory Comput.* **2013**, *9*, 4526–4541.

(9) Filatov, M. Spin-restricted ensemble-referenced Kohn-Sham method: basic principles and application to strongly correlated ground and excited states of molecules. *WIREs Comput. Mol. Sci.* **2015**, *5*, 146–167.

(10) Filatov, M. In *Density-functional methods for excited states*; Ferré, N., Filatov, M., Huix-Rotllant, M., Eds.; Top. Curr. Chem.; Springer: Heidelberg, 2016; Vol. 368; pp 97–124.

(11) Valone, S. M. A one-to-one mapping between one-particle densities and some n-particle ensembles. *J. Chem. Phys.* **1980**, *73*, 4653–4655.

(12) Lieb, E. H. Density functionals for Coulomb systems. *Int. J. Quantum Chem.* **1983**, *24*, 243–277.

(13) Perdew, J. P.; Parr, R. G.; Levy, M.; Balduz Jr., J. L. Density-Functional Theory for Fractional Particle Number: Derivative Discontinuities of the Energy. *Phys. Rev. Lett.* **1982**, *49*, 1691–1694.

(14) Englisch, H.; Englisch, R. Hohenberg-Kohn Theorem and Non-V-Representable Densities. *Physica* **1983**, *A121*, 253–268.

(15) Englisch, H.; Englisch, R. Exact Density Functionals for Ground-State Energies. I. General Results. *Phys. Stat. Sol. (b)* **1984**, *123*, 711–721.

(16) Englisch, H.; Englisch, R. Exact Density Functionals for Ground-State Energies II. Details and Remarks. *Phys. Stat. Sol. (b)* **1984**, *124*, 373–379.

(17) Gross, E. K. U.; Oliveira, L. N.; Kohn, W. Rayleigh-Ritz variational principle for ensembles of fractionally occupied states. *Phys. Rev. A* **1988**, *37*, 2805–2808.

(18) Gross, E. K. U.; Oliveira, L. N.; Kohn, W. Density-functional theory for ensembles of fractionally occupied states. I. Basic formalism. *Phys. Rev. A* **1988**, *37*, 2809–2820.

(19) Oliveira, L. N.; Gross, E. K. U.; Kohn, W. Density-functional theory for ensembles of fractionally occupied states. II. Application to the He atom. *Phys. Rev. A* **1988**, *37*, 2821–2833.

(20) Oliveira, L. N.; Gross, E. K. U.; Kohn, W. Ensemble-Density Functional Theory. *Int. J. Quantum Chem.: Quantum Chem. Symp.* **1990**, *24*, 707–716.

(21) Filatov, M.; Liu, F.; Martínez, T. J. Analytical derivatives of the individual state energies in ensemble density functional theory method. I. General formalism. *J. Chem. Phys.* **2017**, *147*, 034113.

(22) Ha, J.-K.; Lee, I. S.; Min, S. K. Surface Hopping Dynamics beyond Nonadiabatic Couplings for Quantum Coherence. *J. Phys. Chem. Lett.* **2018**, *9*, 1097–1104.

(23) Hunter, G. Conditional probability amplitudes in wave mechanics. *Int. J. Quantum Chem.* **1975**, *9*, 237–242.

(24) Abedi, A.; Maitra, N. T.; Gross, E. K. U. Exact factorization of the time-dependent electron-nuclear wave function. *Phys. Rev. Lett.* **2010**, *105*, 123002.

(25) Abedi, A.; Maitra, N. T.; Gross, E. K. U. Correlated electron-nuclear dynamics: Exact factorization of the molecular wave-function. *J. Chem. Phys.* **2012**, *137*, 22A530.

(26) Abedi, A.; Agostini, F.; Suzuki, Y.; Gross, E. K. U. Dynamical steps that bridge piecewise adiabatic shapes in the exact time-dependent potential energy surface. *Phys. Rev. Lett.* **2013**, *110*, 263001.

(27) Agostini, F.; Abedi, A.; Suzuki, Y.; Min, S. K.; Maitra, N. T.; Gross, E. K. U. The exact electronic back-reaction on classical nuclei in non-adiabatic charge transfer. *J. Chem. Phys.* **2015**, *142*, 084303.

(28) Tully, J. C. Molecular dynamics with electronic transitions. *J. Chem. Phys.* **1990**, *93*, 1061.

(29) Granucci, G.; Persico, M.; Zoccante, A. Including quantum decoherence in surface hopping. *J. Chem. Phys.* **2010**, *133*, 134111.

(30) Hammes-Schiffer, S.; Tully, J. C. Proton transfer in solution: Molecular dynamics with quantum transitions. *J. Chem. Phys.* **1994**, *101*, 4657–4667.

(31) Ufimtsev, I. S.; Martínez, T. J. Quantum Chemistry on Graphical Processing Units. 1. Strategies for two-electron integral evaluation. *J. Chem. Theory Comput.* **2008**, *4*, 222–231.

(32) Ufimtsev, I. S.; Martínez, T. J. Quantum Chemistry on Graphical Processing Units. 2. Direct Self-Consistent-Field (SCF) Implementation. *J. Chem. Theory Comput.* **2009**, *5*, 1004–1015.

(33) Ufimtsev, I. S.; Martínez, T. J. Quantum Chemistry on Graphical Processing Units. 3. Analytical Energy Gradients and First Principles Molecular Dynamics. *J. Chem. Theory Comput.* **2009**, *5*, 2619–2628.

(34) Ufimtsev, I. S.; Martínez, T. J. Graphical Processing Units for Quantum Chemistry. *Comput. Sci. Eng.* **2008**, *10*, 26–34.

(35) Titov, A. V.; Ufimtsev, I. S.; Luehr, N.; Martínez, T. J. Generating Efficient Quantum Chemistry Codes for Novel Architectures. *J. Chem. Theory Comput.* **2013**, *9*, 213–221.

(36) Song, C.; Wang, L.-P.; Martínez, T. J. Automated Code Engine for Graphical Processing Units: Application to the Effective Core Potential Integrals and Gradients. *J. Chem. Theory Comput.* **2016**, *12*, 92–106.

(37) Krishnan, R.; Binkley, J. S.; Seeger, R.; Pople, J. A. Self-consistent molecular orbital methods. XX. A basis set for correlated wave functions. *J. Chem. Phys.* **1980**, *72*, 650–654.

(38) Becke, A. D. Density-Functional Exchange-Energy Approximation with Correct Asymptotic Behavior. *Phys. Rev. A* **1988**, *38*, 3098–3100.

(39) Lee, C.; Yang, W.; Parr, R. G. Development of the Colle-Salvetti Correlation-Energy Formula into a Functional of the Electron Density. *Phys. Rev. B* **1988**, *37*, 785–789.

(40) Becke, A. D. A New Mixing of Hartree-Fock and Local Density-Functional Theories. *J. Chem. Phys.* **1993**, *98*, 1372–1377.

(41) Kästner, J.; Carr, J. M.; Keal, T. W.; Thiel, W.; Wander, A.; Sherwood, P. DL-FIND: An Open-Source Geometry Optimizer for Atomistic Simulations. *J. Phys. Chem. A* **2009**, *113*, 11856–11865.

(42) Levine, B.; Coe, J. D.; Martínez, T. J. Optimizing conical intersections without derivative coupling vectors: application to multistate multireference second-order perturbation theory (MS-CASPT2). *J. Phys. Chem. B* **2008**, *112*, 405–413.

(43) Jónsson, H.; Mills, G.; Jacobsen, K. W. In *Classical and Quantum Dynamics in Condensed Phase Simulations*; Berne, B. J., Ciccotti, G., Coker, D. F., Eds.; World Scientific: Singapore, 1998; Chapter 16, pp 385–404.

(44) Oppenheim, I.; Ross, J. Temperature Dependence of Distribution Functions in Quantum Statistical Mechanics. *Phys. Rev.* **1957**, *107*, 28–32.

(45) Davies, R. W.; Davies, K. T. R. On the Wigner Distribution Function for an Oscillator. *Ann. Phys.* **1975**, *89*, 261–273.

(46) Lan, Z.; Lu, Y.; Weingart, O.; Thiel, W. Nonadiabatic Decay Dynamics of a Benzylidene Malononitrile. *J. Phys. Chem. A* **2012**, *116*, 1510–1518.

(47) Hermann, G.; Pohl, V.; Tremblay, J. C.; Paulus, B.; Hege, H.-C.; Schild, A. ORBKIT: A Modular Python Toolbox for Cross-Platform Postprocessing of Quantum Chemical Wavefunction Data. *J. Comput. Chem.* **2016**, *37*, 1511–1520.

(48) Nangia, S.; Jasper, A. W.; Miller, T. F.; Truhlar, D. G. Army ants algorithm for rare event sampling of delocalized nonadiabatic transitions by trajectory surface hopping and the estimation of sampling errors by the bootstrap method. *J. Chem. Phys.* **2004**, *120*, 3586–3597.